

# Stacked Graphene- $\text{Al}_2\text{O}_3$ Nanopore Sensors for Sensitive Detection of DNA and DNA–Protein Complexes

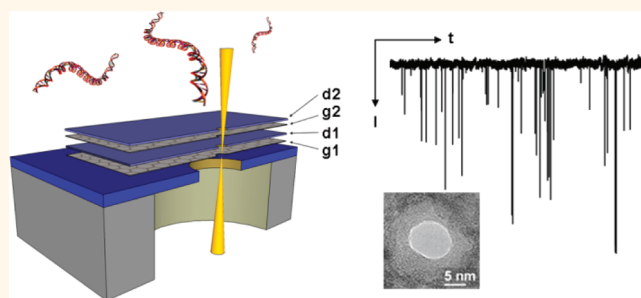
Bala Murali Venkatesan,<sup>†,\*</sup> David Estrada,<sup>†,\*</sup> Shouvik Banerjee,<sup>‡,§</sup> Xiaozhong Jin,<sup>⊥,||</sup> Vincent E. Dorgan,<sup>†,\*</sup> Myung-Ho Bae,<sup>†,\*</sup> Narayana R. Aluru,<sup>⊥,||</sup> Eric Pop,<sup>†,‡,||</sup> and Rashid Bashir<sup>†,‡,||,#,\*</sup>

<sup>†</sup>Department of Electrical and Computer Engineering, <sup>‡</sup>Micro and Nanotechnology Lab, <sup>§</sup>Department of Materials Science and Engineering, <sup>⊥</sup>Department of Mechanical Science and Engineering, <sup>||</sup>Beckman Institute, <sup>#</sup>Department of Bioengineering, University of Illinois at Urbana–Champaign, Illinois, United States

Nanopore-based DNA analysis is an emerging technique that involves electrophoretically driving DNA molecules through a nanoscale pore in solution and monitoring the corresponding change in ionic pore current. This versatile approach permits the label-free, amplification-free analysis of charged polymers (single-stranded DNA, double-stranded DNA and RNA) ranging in length from single nucleotides to kilobase-long genomic DNA fragments with sub-nanometer resolution. Recent advances in nanopores suggest that this low-cost, highly scalable technology could lend itself to the development of third-generation DNA sequencing technologies, promising rapid and reliable sequencing of the human diploid genome for under \$1000.<sup>1,2</sup>

Solid-state nanopores in graphene, in particular, hold much promise, as the spacing between nucleotides in single-stranded DNA (ssDNA) is 0.32–0.52 nm, which is comparable to the “thickness” of single- and bilayer graphene (0.34–0.68 nm), making this material very attractive for electronic DNA sequencing. Graphene is an atomically thin sheet of carbon atoms arranged into a two-dimensional honeycomb lattice, with remarkable mechanical, electrical, and thermal properties.<sup>3</sup> The formation of nanopores in suspended monolayer and multilayer graphene membranes and the transport of double-stranded DNA (dsDNA) through these structures have been recently demonstrated.<sup>4–6</sup> Moreover, subtle structural features in the translocating molecule (folded *versus* unfolded dsDNA) could be discerned<sup>4–6</sup> with a theoretical spatial resolution of a single nucleotide,<sup>4</sup> demonstrating the potential sensitivity of a graphene nanopore platform.<sup>4–6</sup> Experimentally achieving this resolution however is challenging for two

## ABSTRACT



We report the development of a multilayered graphene- $\text{Al}_2\text{O}_3$  nanopore platform for the sensitive detection of DNA and DNA–protein complexes. Graphene- $\text{Al}_2\text{O}_3$  nanolaminate membranes are formed by sequentially depositing layers of graphene and  $\text{Al}_2\text{O}_3$ , with nanopores being formed in these membranes using an electron-beam sculpting process. The resulting nanopores are highly robust, exhibit low electrical noise (significantly lower than nanopores in pure graphene), are highly sensitive to electrolyte pH at low KCl concentrations (attributed to the high buffer capacity of  $\text{Al}_2\text{O}_3$ ), and permit the electrical biasing of the embedded graphene electrode, thereby allowing for three terminal nanopore measurements. In proof-of-principle biomolecule sensing experiments, the folded and unfolded transport of single DNA molecules and RecA-coated DNA complexes could be discerned with high temporal resolution. The process described here also enables nanopore integration with new graphene-based structures, including nanoribbons and nanogaps, for single-molecule DNA sequencing and medical diagnostic applications.

**KEYWORDS:** nanopore · graphene · DNA · translocation · sequencing

reasons: (1) the high DNA translocation velocity in graphene nanopores ( $>40$  nucleotides/ $\mu\text{s}$ )<sup>4</sup> pushes the detector bandwidth requirements to the MHz region, which precludes the measurement of pico-ampere steps in ionic current, and (2) high  $1/f$  noise in graphene nanopores can reduce the detector signal-to-noise ratio and potentially prohibit the direct measurement of individual nucleotides using ionic current. As a result,

\* Address correspondence to rbashir@illinois.edu.

Received for review October 2, 2011 and accepted December 13, 2011.

Published online December 13, 2011  
10.1021/nn203769e

© 2011 American Chemical Society

the application of graphene nanopores to direct, real-time sequencing will likely require novel architectures that add functionality to the nanopore. Theoretical studies proposing the use of semiconducting graphene nanoribbons<sup>7,8</sup> and graphene tunnel junctions or nanogaps<sup>9,10</sup> have shown much promise; however the fabrication of such structures remains challenging and will likely require a multilayered graphene–dielectric architecture.

Here, we report the fabrication of a graphene- $\text{Al}_2\text{O}_3$  nanolaminate membrane with a single nanopore for the highly sensitive detection of individual DNA molecules and DNA–protein complexes. Nanopores in this multilayered architecture are highly robust, exhibit low electrical  $1/f$  noise (a significant improvement over nanopores in graphene alone), are highly sensitive to solution pH at low electrolyte concentrations (more so than nanopores in SiN), and permit the electrical biasing of the embedded graphene electrode, thereby allowing for three terminal nanopore measurements. The enhanced pH response and low  $1/f$  electrical noise properties are attributed to  $\text{Al}_2\text{O}_3$  interleaved among layers of graphene, which further helps to reduce charge transfer at the fluid interface and minimizes graphene degradation, making this system ideal for low-noise DNA translocation measurements. The electroactivity and degradation of exposed exfoliated monolayer and bilayer graphene in electrolyte were previously reported.<sup>11</sup> In proof-of-principle biomolecule translocation experiments, we demonstrate the folded and unfolded translocation of 48.5 kbp  $\lambda$  dsDNA and dsDNA coated by recombination protein A (RecA) through graphene- $\text{Al}_2\text{O}_3$  nanopores, the protein–DNA complex exhibiting significantly deeper ionic current blockades than native dsDNA. The methodology described here could be extended to the fabrication of a vertical platform with any number of stacked graphene electrodes distributed along the length of the nanopore channel, each independently biased and of thickness comparable to the internucleotide spacing in dsDNA. Furthermore each graphene layer could be patterned using electron beam or nanoimprint lithography to form stacked nanoribbon and nanogap architectures for the controlled transport of DNA, analogous to the base-by-base ratcheting of DNA through a nanopore transistor as proposed by IBM.<sup>12</sup> Developing such methods to slow DNA transport are critical in overcoming the high DNA translocation velocities currently limiting the utility of solid-state nanopores in DNA sequencing and diagnostic applications.<sup>2</sup>

## RESULTS AND DISCUSSIONS

Graphene is chosen as the electrode material in these studies due to its single-atom thickness and excellent mechanical and electrical properties<sup>13</sup> (low resistivity, high breakdown current density<sup>14</sup>). Unlike ultrathin (<10 nm) noble metal films on  $\text{SiO}_2$ , which are

typically discontinuous,<sup>15</sup> prohibitively resistive, unstable, and prone to electromigration (a phenomenon that degrades atomically thin Au electrodes<sup>16</sup>), graphene monolayers and bilayers are significantly more stable. Graphene is also ideal for making nanogaps and nanoribbons for DNA sequencing applications, with simulations reporting nucleotide-specific electron tunneling currents in nanogaps of widths 1.0–1.5 nm.<sup>9</sup> Furthermore, the single-atom thickness of graphene permits the fabrication of nanopores in this material with relative ease.<sup>5,6</sup> In graphene, the displacement threshold energy for the ejection of an  $\text{sp}^2$ -bound C atom (three bonds) is 17 eV, or 15 eV for C sites with a neighboring vacancy (two bonds).<sup>17</sup> At a graphene pore edge where atoms may have several vacant nearest-neighbor sites, the displacement threshold energy may be even less; thus the sputtering of nanopores in graphene could be considered a relatively low energy process (achieved with beam energies as low as 80 keV). Transmission electron microscope (TEM)-based sputtering of nanopores in metal thin films, however, is more challenging. Nanopore formation in 10–30 nm thick continuous Cr and Au films has been demonstrated; however pores in these films lack control in terms of size and shape, require very high electron beam energies (200–300 keV) to form, and are often unstable.<sup>18</sup> For example, the displacement threshold energy for Au is 35 eV,<sup>19</sup> more than double the reported value for C atoms in graphene, making nanopore fabrication in Au a difficult and relatively high electron energy process.

The fabrication of multilayered graphene- $\text{Al}_2\text{O}_3$  nanopore structures is outlined in Figure 1a–d. The process involves first forming a 300–350 nm diameter aperture in a  $\sim 70$  nm thick free-standing  $\text{Al}_2\text{O}_3$  membrane using a focused ion beam (FIB) tool (Figure 1a, e).<sup>20,21</sup> Graphene grown *via* chemical vapor deposition (CVD) is next transferred onto this substrate (Figure 1b), this layer being referred to as g1. The substrate is next annealed in a furnace at 400 °C under Ar/ $\text{H}_2$  flow to remove any residual PMMA,<sup>22</sup> and the quality of the transferred film is inspected using Raman spectroscopy and electron diffraction imaging. The ratio of the 2D to G peak ( $I_{2D}/I_G$ ) in the Raman spectra of Figure 1f and the 6-fold symmetry observed in the electron diffraction pattern (Figure 1g) from the suspended graphene membrane confirms primarily monolayer and bilayer coverage. These results are in good agreement with the large area monolayer thicknesses reported by Li *et al.*<sup>23</sup> using a similar CVD growth process.<sup>24</sup> Next, a metallic Al seed layer of thickness 1.5 nm is evaporated onto g1. Upon oxidation in air, this seed layer promotes the conformal deposition of  $\text{Al}_2\text{O}_3$  and prevents non-uniform dielectric nucleation.<sup>25,26</sup> A 6.5 nm layer of  $\text{Al}_2\text{O}_3$  (dielectric layer 1, or d1) is next deposited on this seed layer by atomic layer deposition (ALD; see Methods for process parameters).

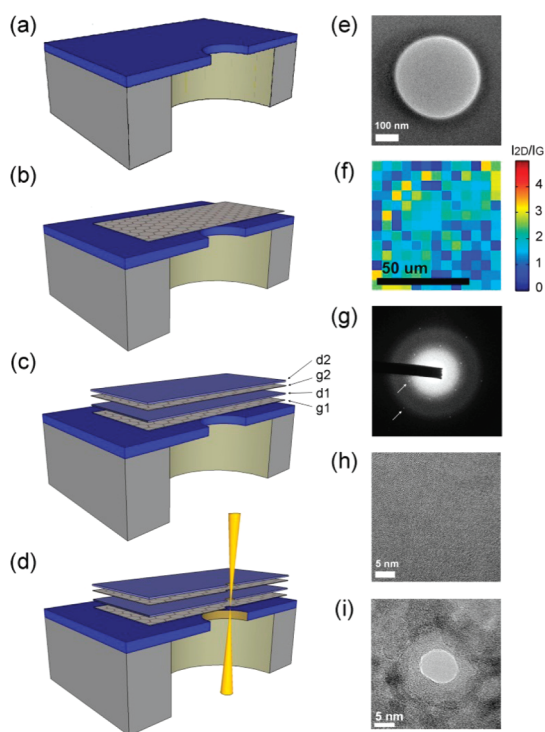


**Figure 1.** Fabrication of multilayered graphene- $\text{Al}_2\text{O}_3$  membranes with single nanopores. (a) A 300–350 nm diameter pore is first formed in a 70 nm thick  $\text{Al}_2\text{O}_3$  membrane using a focused ion beam. (b) CVD grown graphene is next transferred onto the  $\text{Al}_2\text{O}_3$  surface (g1) including over the pore region, thereby forming a suspended graphene membrane. (c) Metallic Al is evaporated on the graphene, followed by the deposition of ALD  $\text{Al}_2\text{O}_3$  (d1). A second graphene layer is then transferred (g2), and a Ti/Au contact evaporated at the edge of the g2 layer. The second Al seed/ $\text{Al}_2\text{O}_3$  dielectric layer is then deposited (d2). (d) A nanopore is formed in this graphene–dielectric stack using a focused convergent electron beam. (e) TEM image of the  $\sim 350$  nm diameter FIB pore after step (a). (f) Large-area Raman map of g1 showing primarily monolayer to bilayer coverage. (g) TEM diffraction pattern from the suspended graphene membrane following step (b). (h) TEM image of the graphene- $\text{Al}_2\text{O}_3$  suspended membrane following step (c). (i) TEM image of a  $\sim 8.9$  nm diameter nanopore formed in the graphene- $\text{Al}_2\text{O}_3$  membrane using a focused electron beam.

We note that the g1 layer serves as a mechanical support for subsequent layers. Without this mechanical support, the d1 layer as deposited would simply coat the inside of the FIB pore, as ALD is a conformal deposition process. ALD is the process of choice here, as it allows for sub-nanometer level control over the thickness of the deposited film, and the low temperature nature of this process ( $\sim 250$  °C) makes it compatible with previously deposited graphene and metal layers. In contrast, low-pressure chemical vapor deposition (LPCVD) of SiN is not compatible with our process, as the LPCVD technique lacks sub-nanometer control over film thickness and the elevated deposition temperature ( $\sim 800$  °C) could degrade existing graphene layers on the substrate. Moreover, the choice of  $\text{Al}_2\text{O}_3$  as the dielectric material here is based on previous studies that have shown that (1) low  $1/f$  electrical

noise is observed in  $\text{Al}_2\text{O}_3$  nanopores;<sup>20</sup> (2) effective gate isolation can be achieved with as little as 5 nm of  $\text{Al}_2\text{O}_3$ ;<sup>27</sup> (3) strong pH response is observed in  $\text{Al}_2\text{O}_3$ -coated graphene transistors versus graphene alone, which is insensitive to solution pH;<sup>28</sup> and (4) strong electrostatic interactions between  $\text{Al}_2\text{O}_3$  (positively charged) and negatively charged dsDNA at pH 7.5 can help reduce DNA translocation velocity.<sup>29</sup>

The entire process (graphene growth and transfer, seed layer deposition, and ALD  $\text{Al}_2\text{O}_3$ ) is then repeated once more, resulting in a multilayered graphene/ $\text{Al}_2\text{O}_3$  stack, as shown in Figure 1c. The membrane thickness post-fabrication is  $\sim 20$  nm in the 300–350 nm diameter aperture area. Notably, the g2 layer serves as the active device layer. This layer is insulated on both sides by  $\sim 6.5$  nm of ALD  $\text{Al}_2\text{O}_3$  and as a result can be biased with minimal current leakage, serving as the gate electrode in the stacked architecture. A TEM image of the suspended membrane stack is shown in Figure 1h.

Finally, a focused convergent electron beam from a field-emission gun TEM is used to form a single nanopore in the stack, as shown in Figure 1d. By tuning the beam current density and drill time, pores of varying diameter can be sputtered in these membranes and sculpted with sub-nanometer precision. Figure 1i shows a TEM image of an 8.9 nm diameter nanopore formed using this technique in a multilayered graphene- $\text{Al}_2\text{O}_3$  membrane. This process also permits the electrical contacting of the g2 layer, enabling the formation of a nanopore with an embedded atomically thin graphene electrode. This is achieved by evaporating a Ti/Au pad (5 nm/250 nm thick) over the edge of the g2 layer prior to the second Al seed layer and  $\text{Al}_2\text{O}_3$  dielectric (d2) deposition steps. Previous nanopore ionic field effect transistor (IFET) studies have typically used a thick ( $>30$  nm) TiN or Cr electrode embedded in the nanopore to modulate ionic pore current.<sup>30–33</sup> In contrast, the approach described here enables the formation of a stacked architecture with multiple ultrathin graphene electrodes analogous to the architecture proposed by IBM.<sup>12</sup> Following nanopore formation in the multilayer stack, the chip is  $\text{O}_2$  plasma treated on the Si trench side for 1 min at 50 W to render the surface hydrophilic and epoxied (Kwikcast from World Precision Instruments) to a custom-designed printed circuit board (PCB).

The evaporated Ti/Au pads on the g2 layer are contacted using indium wires (Figure 2a). The resistance measured across pads 1 and 2 is typically in the range 5–15 k $\Omega$ , confirming the presence of a conductive g2 layer after nanopore fabrication and consistent with our typical CVD graphene resistivity values.<sup>24,34</sup> The chip mounted on the PCB is next inserted into a custom-designed fluidic setup, as shown in Figure 2b.

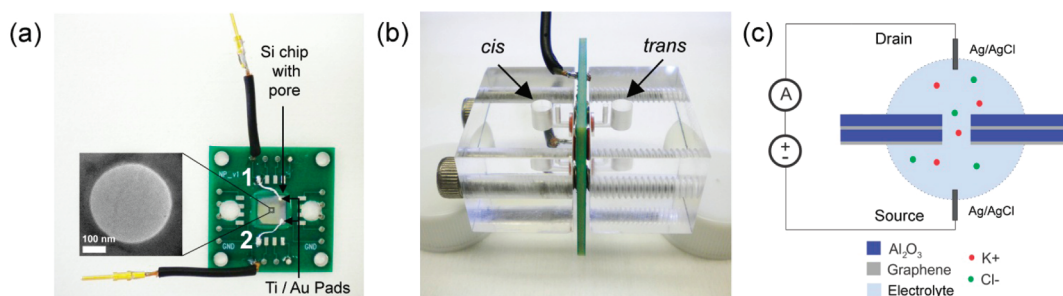


Figure 2. Electrical and fluidic setup. (a) Graphene- $\text{Al}_2\text{O}_3$  nanopore chip mounted on a PCB. Ti/Au pads with indium contacts are shown. (b) Nanopore PCB mounted in a custom-designed fluidic setup. O-rings electrically isolate the *cis* and *trans* chambers containing the electrolyte from the Ti/Au pads. (c) Schematic of the experimental setup.

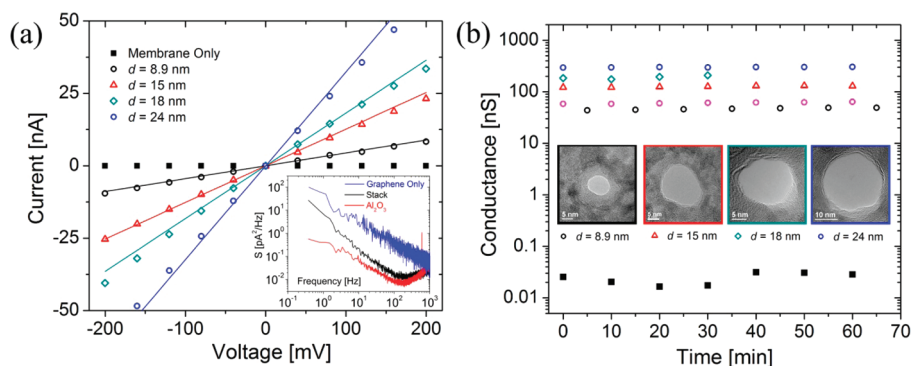


Figure 3. Graphene- $\text{Al}_2\text{O}_3$  nanopore electrical characterization. (a) Measured current–voltage ( $I$ – $V$ ) response from graphene- $\text{Al}_2\text{O}_3$  nanopores of various diameter (symbols) in 1 M KCl, 10 mM Tris, 1 mM EDTA, pH 8 electrolyte. Linear characteristics are observed. Measured values are in good agreement with numerical simulations (solid lines), computed using eqs 3–9 from the Methods section.  $I$ – $V$  response of a multilayer membrane without a nanopore is also shown (solid squares). (Inset) Noise power spectra from nanopores of diameter 8–9 nm in graphene only, a multilayered graphene- $\text{Al}_2\text{O}_3$  stack, and  $\text{Al}_2\text{O}_3$  alone. Noise spectral components exhibit the highest amplitude in the pure graphene case, resulting from high  $1/f$  noise. In comparison,  $1/f$  noise in graphene- $\text{Al}_2\text{O}_3$  nanopores is significantly less and is comparable to that observed in  $\text{Al}_2\text{O}_3$  nanopores. (b) Conductance stability *versus* time for graphene- $\text{Al}_2\text{O}_3$  nanopores from (a) with TEM images of each pore inset. Stable pore conductance is observed for over 60 min. Stability of a membrane without a nanopore is also shown (solid squares).

Conductive electrolyte (1 M KCl, 10 mM Tris, 1 mM EDTA, pH 8) is inserted into each fluidic reservoir, and a potential is applied across the *cis* and *trans* chambers using Ag/AgCl electrodes, resulting in the flow of ions through the nanopore. The reservoir design permits the electrical isolation of the Ti/Au pads from the conductive electrolyte. A schematic of the experimental setup is shown in Figure 2c. The g2 layer is left floating in the following electrical characterization and biomolecule transport experiments.

The current *versus* voltage ( $I$ – $V$ ) characteristics of multiple graphene- $\text{Al}_2\text{O}_3$  nanopores in 1 M KCl, 10 mM Tris, 1 mM EDTA, pH 8, are shown in Figure 3a. Linear  $I$ – $V$  characteristics are observed in all cases, suggesting a symmetric nanopore structure as previously reported in simple  $\text{Al}_2\text{O}_3$  nanopores.<sup>20,21</sup> Figure 3a illustrates measured  $I$ – $V$  characteristics (symbols) from an 8.9, 15, 18, and 24 nm diameter nanopore with corresponding TEM images inset in Figure 3b. The solid lines in Figure 3a represent simulated pore currents solved using numerical techniques (see Methods for full description). Briefly, the coupled Poisson–Nernst–Planck equations and Navier–Stokes equations

for fluid flow in the nanopore are solved to obtain the local electric potential, ion concentration, velocity, and pressure profiles. The current through the nanopore channel is calculated by integrating the ionic fluxes over the cross-sectional area of the channel (pore area extracted from TEM images) such that

$$I = \int_S \sum_i z_i F \Gamma_i \cdot \mathbf{n} dS \quad (1)$$

where  $S$  is the cross-sectional area of the pore,  $z_i$  is the valence of the  $i$ th species (one for both  $\text{K}^+$  and  $\text{Cl}^-$ ),  $F$  is Faraday's constant,  $\Gamma_i$  is the total flux of the  $i$ th species through the pore accounting for diffusion, electromigration, and convection, and  $\mathbf{n}$  is the vector normal to the pore surface. Good agreement between experimental (symbols) and simulated results (solid lines) is observed for all pores in 1 M KCl. Note, at pH 8, a low surface charge density ( $|\sigma| = 10 \text{ mC/m}^2$ ) is assumed in the nanopore in all simulations. This assumption is reasonable, as the effect of surface charge on the ionic current is negligible in 1 M KCl, given the Debye screening length  $\kappa^{-1} \approx 0.3 \text{ nm} \ll d_{\text{pore}}$ , where  $\kappa^2 = (2e^2 n_{\text{KCl}}) / (k_B T \epsilon \epsilon_0)$ . In this equation,  $n_{\text{KCl}}$  represents the number



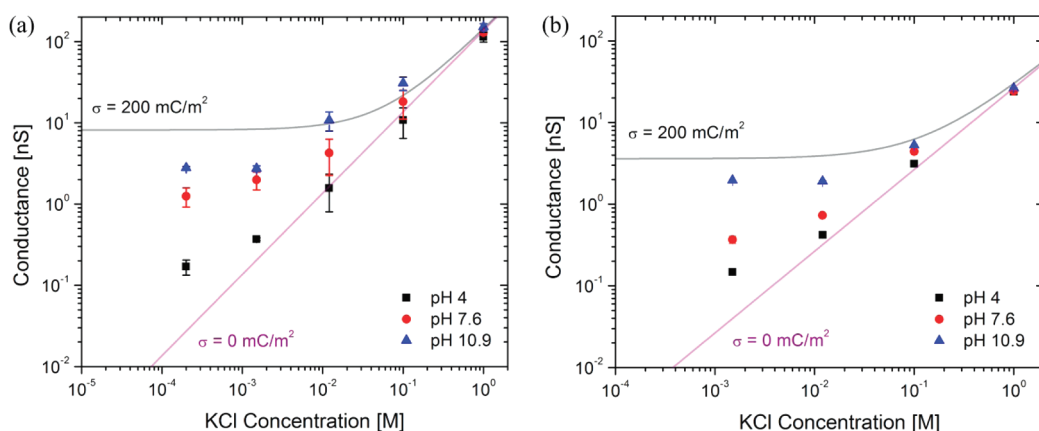


**Figure 4.** Nanopore pH response. (a) Conductance of a  $17 \pm 1$  nm diameter graphene- $\text{Al}_2\text{O}_3$  nanopore versus KCl concentration for different electrolyte pH values. (b) The effect of pore size: conductance of an  $8 \pm 0.5$  nm diameter graphene- $\text{Al}_2\text{O}_3$  pore as a function of KCl concentration and electrolyte pH. Pore conductance is highly pH-dependent and deviates significantly from bulk behavior as KCl concentration is reduced due to surface charge effects. The solid lines depict the calculated conductance (eq 2) of an uncharged nanopore exhibiting bulk behavior ( $\sigma = 0 \text{ mC/m}^2$ ) and a channel with a high surface charge density of  $\sigma = 200 \text{ mC/m}^2$ .

density of  $\text{K}^+$  and  $\text{Cl}^-$  ions,  $e$  the elementary charge,  $k_B$  the Boltzmann constant,  $T$  the temperature;  $\epsilon$  and  $\epsilon_0$  are the relative permittivity of the electrolyte and permittivity of free space, respectively. Electroosmotic flows resulting from condensed counterions on the charged pore surface should also be negligible under these conditions.<sup>35</sup>

The inset of Figure 3a shows the low-frequency electrical noise from nanopores of diameter 8–9 nm formed in multilayered graphene  $\text{Al}_2\text{O}_3$  membranes versus membranes of either graphene alone or  $\text{Al}_2\text{O}_3$  at an applied voltage of 200 mV (also see supplementary Figure 1 for noise comparison). The low-frequency  $1/f$  noise observed in the stack architecture is comparable in magnitude to pores in  $\text{SiN}$  and  $\text{Al}_2\text{O}_3$ ,<sup>5,20</sup> but is significantly less than in pure graphene nanopores, where high  $1/f$  noise is attributed to incomplete wetting of the surface likely due to the hydrophobicity of graphene.<sup>5</sup> Minimizing this low-frequency  $1/f$  noise is integral to maximizing the sensitivity and signal-to-noise ratio of a nanopore. Figure 3b illustrates the stability of graphene- $\text{Al}_2\text{O}_3$  membranes containing a single nanopore; pore conductance is plotted as a function of time for the devices in Figure 3a. Stable conductance values are observed for over 60 min, confirming the chemical and mechanical stability of each device in conductive electrolyte. The conductance versus time data for a graphene- $\text{Al}_2\text{O}_3$  membrane with no pore (black solid squares) is also shown. The nonzero conductance is likely due to current leakage paths through pinholes in the dielectric and defects in the CVD graphene, analogous to leakage currents observed in  $\text{TiO}_2$ -coated graphene membranes.<sup>5</sup> However, these leakage currents are 3 to 4 orders of magnitude less than the ionic current through the nanofabricated pore and are therefore negligible.

Our results also suggest that it should be possible to electrically bias the embedded graphene g2 layer in the nanopore. Supplementary Figure 2 (Figure S2) shows a schematic of the three terminal graphene nanopore architecture. The graphene gate and drain are electrically connected to reduce leakage currents across the gate–drain terminals with nanopore current being measured across the source and drain using Ag/AgCl electrodes. Biasing the g2 layer can indeed modulate the ionic current through the nanopore at low electrolyte concentrations, as seen in Supplementary Figure 3 (analogous to current modulation in a FET using the gate electrode). Figure S3 shows nanopore current ( $I$ ) versus source–drain voltage ( $V_{s,d}$ ) as a function of KCl concentration at pH 7.6. Applied voltages across the gate–source were  $\leq 100$  mV, corresponding to an electric field of  $\sim 0.15$  MV/cm, well below the critical breakdown field of  $\text{Al}_2\text{O}_3$  (4–5 MV/cm). In general, higher conductance is observed at pH 7.6 with the gate connected relative to the floating gate case at all KCl concentrations examined. The current enhancement is most pronounced at low salt concentrations due to electrostatic modulation of the Debye screening layer in the pore. Notably, the Debye screening length in 1 M KCl is only  $\sim 0.3$  nm, but in 10 mM KCl is  $\sim 3$  nm and is comparable to the  $\sim 19$  nm diameter of the nanopore used in this experiment. Similar trends have been observed at low electrolyte concentrations in nanopore arrays using an embedded TiN gate electrode.<sup>33</sup> The application of local potentials in the pore via this third electrode may also prove useful in slowing or trapping DNA molecules in the pore. The viability of these concepts needs to be explored further.

The surface charge characteristics and pH response of graphene- $\text{Al}_2\text{O}_3$  nanopores are shown in Figure 4. Pore conductance versus electrolyte concentration is

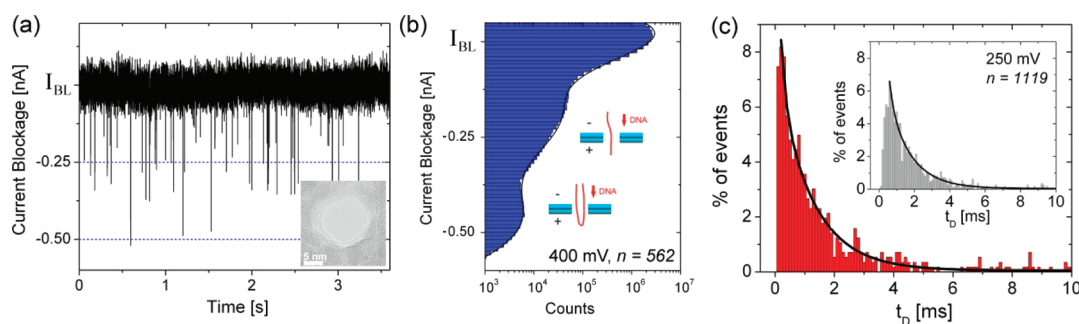


**Figure 5.**  $\lambda$ -DNA transport. (a) Sample current traces showing the transport of 48.5 kbp  $\lambda$ -DNA through an 11.3 nm diameter graphene- $\text{Al}_2\text{O}_3$  nanopore at an applied voltage of 400 mV in 1 M KCl, 10 mM Tris, 1 mM EDTA, pH 10 electrolyte. Each downward spike from the baseline current level ( $I_{\text{BL}}$ ) corresponds to the transport of a single  $\lambda$ -DNA molecule. (Inset) TEM image of the nanopore; scale bar is 5 nm. (b) Current blockage histogram showing two distinct current peaks, corresponding to the unfolded and folded transport of  $\lambda$ -DNA. The histogram is composed of  $n = 562$  separate translocation events at 400 mV. (c) Event translocation time ( $t_{\text{D}}$ ) histogram at 400 mV with a biexponential function fitted to the data. Mean  $t_{\text{D}} = 1.81 \pm 2.77$  ms at 400 mV. (Inset) Event translocation time ( $t_{\text{D}}$ ) histogram at 250 mV constructed from  $n = 1119$  separate  $\lambda$ -DNA transport events. Mean  $t_{\text{D}} = 2.66 \pm 4.08$  ms at 250 mV, confirming voltage-dependent DNA transport through the nanopore.

shown in Figure 4a and b for  $17 \pm 1$  and  $8 \pm 0.5$  nm diameter nanopores, respectively, with the g2 layer in both cases left floating. Pore conductance is not dependent on pH at high salt concentration (1 M KCl), confirming that surface charge effects are indeed negligible under these conditions. As salt concentration is reduced however, surface effects become more prominent and pore conductance plateaus, this effect being more pronounced at high pH. These results can be qualitatively described using a simple geometric model that approximates pore conductance,<sup>35</sup>  $G_{\text{pore}}$ , as follows:

$$G_{\text{pore}} = \frac{\pi}{4} \frac{d_{\text{pore}}^2}{L_{\text{pore}}} \left[ (\mu_{\text{K}} + \mu_{\text{Cl}}) n_{\text{KCl}} e + \mu_{\text{K}} \frac{4}{d_{\text{pore}}} \left| \frac{\sigma}{d_{\text{pore}}} \right| \right] \quad (2)$$

with  $d_{\text{pore}}$  representing nanopore diameter,  $L_{\text{pore}}$  the length of the cylindrical nanopore, and  $\sigma$  the surface charge density in the nanopore;  $\mu_{\text{K}}$  and  $\mu_{\text{Cl}}$  are the electrophoretic mobilities of potassium and chloride ions, respectively. We use values of  $L_{\text{pore}} = 20$  nm,  $\mu_{\text{K}} = 7.616 \times 10^{-8}$  m<sup>2</sup>/(V s), and  $\mu_{\text{Cl}} = 7.909 \times 10^{-8}$  m<sup>2</sup>/(V s). The first term in eq 2 represents the bulk conductance, and the second term represents the surface charge contribution to the conductance. At high KCl concentrations,  $n_{\text{KCl}} \gg 2\sigma/d_{\text{pore}}e$ , and bulk behavior is observed. Deviations from bulk behavior occur as  $n_{\text{KCl}}$  is lowered. Using this model, upper and lower conductance bounds to the experimental data can be constructed as seen in Figure 4, corresponding to the cases of high ( $\sigma = 200$  mC/m<sup>2</sup>) and low ( $\sigma = 0$  mC/m<sup>2</sup>) surface charge density, respectively.

Our results suggest that surface charge in a graphene- $\text{Al}_2\text{O}_3$  nanopore is both pH- and concentration-dependent, as previously reported in SiN nanopores<sup>35,36</sup> and  $\text{SiO}_2$  nanochannels.<sup>37</sup> The pH response observed here, however, is significantly more pronounced than in bare SiN<sup>36</sup> and  $\text{TiO}_2$ <sup>33</sup> nanopores,

and  $\text{SiO}_2$  nanochannels.<sup>37</sup> The enhanced pH sensitivity is observed in over 10 nanopores of varying diameters and may be attributed to the high surface charge density and buffer capacity of  $\text{Al}_2\text{O}_3$  with supra-Nernstian characteristics being previously reported in  $\text{Al}_2\text{O}_3$ -coated Si field-effect transistors (FETs).<sup>38</sup> Another notable feature in the experimental data is that pore conductance at pH 4 approaches the bulk model ( $\sigma = 0$  mC/m<sup>2</sup>), suggesting that the isoelectric point of a graphene- $\text{Al}_2\text{O}_3$  nanopore is close to 4. This result, though a deviation from planar ALD  $\text{Al}_2\text{O}_3$  surfaces, which typically exhibit an isoelectric point of 8–9, is in good agreement with zeta potential measurements on graphite particles in aqueous solution (isoelectric point of 4.2),<sup>39</sup> suggesting perhaps a C-rich nanopore stoichiometry. Such changes to local nanopore stoichiometry during TEM nanopore fabrication are plausible. Studies by Kimoto *et al.* on  $\text{SiO}_2/\text{Si}_3\text{N}_4/\text{SiO}_2$  nanolaminates<sup>40</sup> showed that O atoms can be dragged between layers by the electron beam, and studies by Wu *et al.*<sup>41,42</sup> demonstrated material mixing in multilayer SiN/ $\text{SiO}_2$  stacks, with liquid-like behavior being observed in the electron beam irradiated nanopore volume. These effects likely give rise to a melded C, Al, and O nanopore surface in our experiments. Stoichiometric variations due to the preferential sputtering of O in  $\text{Al}_2\text{O}_3$  resulting in an Al-rich nanopore environment are also likely.<sup>29</sup> Indeed, these studies confirm that solution pH can be used to effectively modulate the surface potential and conductance of graphene- $\text{Al}_2\text{O}_3$  nanopores. One useful application for this technology may be the detection of localized pH changes during sequencing by synthesis reactions, analogous to the approach adopted by Ion Torrent using Si FETs.<sup>43</sup>

To study the biomolecule transport properties of graphene- $\text{Al}_2\text{O}_3$  nanopores, we performed experiments involving the translocation of  $\lambda$ -DNA, a 48.5 kbp

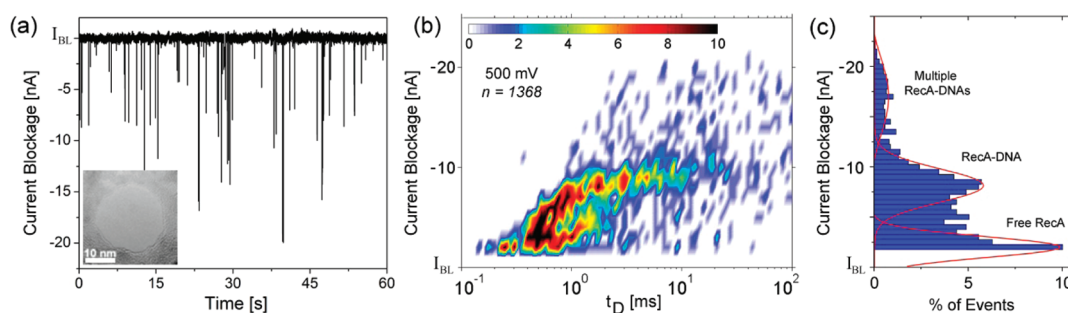


**Figure 6.** RecA-coated DNA transport. (a) Sample current traces showing the transport of RecA-coated dsDNA through a 23 nm diameter graphene- $\text{Al}_2\text{O}_3$  nanopore at an applied voltage of 500 mV in 1 M KCl, 10 mM Tris, 1 mM EDTA, pH 8 electrolyte. The baseline current level is given by  $I_{\text{BL}}$ , and each downward spike corresponds to the transport of either free RecA protein or single/multiple RecA-coated DNA molecules through the pore. (Inset) TEM image of the nanopore; scale bar is 10 nm. (b) Event density plot constructed from 1368 translocation events, showing current blockage versus translocation time ( $t_{\text{D}}$ ) at 500 mV applied bias. Color bar represents number of events. (c) Current blockage histogram at 500 mV. Three distinct peaks are observed with Gaussian fits representing the transport of unbound RecA protein, single RecA-coated DNA molecules, and simultaneous transport of multiple RecA-coated DNA molecules.

long dsDNA fragment. Given the relatively small persistence length of dsDNA ( $l_p = 54 \pm 2$  nm),  $\lambda$ -DNA is expected to assume the shape of a highly coiled ball in high-salt solution with a radius of gyration of  $R_g = (2l_pL)^{1/2} \approx 1.33$   $\mu\text{m}$ . Upon capture in the nanopore, the molecule will elongate and thread through the pore. Figure 5a illustrates current blockades induced by  $\lambda$ -DNA as it translocates through an 11.3 nm diameter graphene- $\text{Al}_2\text{O}_3$  nanopore at an applied voltage of 400 mV in 1 M KCl, 10 mM Tris, 1 mM EDTA, pH 10 electrolyte (higher temporal resolution traces provided in supplementary Figure 4). The  $\lambda$ -DNA concentration used in these experiments is 100 ng/ $\mu\text{L}$ . High-pH electrolyte is used to minimize graphene–DNA interactions<sup>5</sup> and to prevent electrostatic binding of dsDNA to the negatively charged  $\text{Al}_2\text{O}_3$  membrane. These experimental conditions yielded repeatable DNA translocation events. Two distinct blockade levels were observed: a shallow blockade level corresponding to linear dsDNA transport and a deeper blockade level corresponding to folded DNA transport as seen in Figure 5b. The translocation of both folded and unfolded dsDNA structures through SiN nanopores<sup>44,45</sup> and pure graphene nanopores was previously reported.<sup>4–6</sup> The current histogram of Figure 5b is composed of 562 individual DNA translocation events. To confirm that these events are indeed due to DNA translocation and not simply interactions with the pore surface, we probed the effect of voltage on translocation time. Voltage-dependent DNA transport was observed, translocation times,  $t_{\text{D}}$ , decreasing with increasing voltage. Measured mean values for translocation time were  $t_{\text{D}} = 1.81 \pm 2.77$  ms at 400 mV (Figure 5c), and  $t_{\text{D}} = 2.66 \pm 4.08$  ms at 250 mV from  $n = 1119$  events (Figure 5c inset). The broad distribution of translocation times is representative of DNA translocation involving significant interactions with the pore surface.<sup>29,46</sup> These experiments demonstrate that graphene- $\text{Al}_2\text{O}_3$  nanopores are highly sensitive at

detecting not only the presence of a single molecule but also biomolecule secondary structure (folded or unfolded). This system could prove useful in reading sensitive topographic information along the length of a molecule, for example, bound proteins on DNA or RNA secondary structures. In the following section, we show proof-of-principle protein–DNA binding experiments involving RecA-coated DNA.

To study the transport of protein-coated DNA molecules through a nanopore, we use recombination protein A, which is known to form stable nucleoprotein filaments on double-stranded DNA in the presence of magnesium and ATP $\gamma$ S.<sup>47</sup> This model protein plays a central role in homologous recombination and DNA repair in prokaryotes. RecA-coated DNA molecules were prepared and provided by NABsys (Providence, RI, USA) using a process documented previously.<sup>47</sup> The transport of this protein–DNA complex through a graphene- $\text{Al}_2\text{O}_3$  nanopore should induce significantly deeper current blockades relative to native dsDNA, as the effective diameter of this nucleoprotein filament is  $7.5 \pm 0.5$  nm.<sup>47</sup> Figure 6a shows nanopore current versus time for the transport of 8 kbp long RecA-coated dsDNA molecules through a 23 nm diameter graphene- $\text{Al}_2\text{O}_3$  nanopore in 1 M KCl, 10 mM Tris, 1 mM EDTA, pH 8 electrolyte at an applied voltage of 500 mV. Deep current blockades were observed during the translocation of the nucleoprotein filament through the pore with significantly higher signal-to-noise ratio (SNR) relative to native dsDNA (higher temporal resolution traces are shown in supplementary Figure 5). Figure 6b shows an event density plot of current blockage versus translocation time ( $t_{\text{D}}$ ) constructed from 1368 individual RecA-related translocation events; the corresponding event amplitude histogram is shown in Figure 6c. Two categories of transport events are clearly distinguishable: fast, low-amplitude events corresponding to the transport of unbound or free RecA protein as previously shown in SiN

nanopores,<sup>47</sup> and slower, higher amplitude current blockage events corresponding to the transport of single RecA-coated DNA molecules. The translocation time scales for the two event categories described are consistent with that reported in RecA-DNA translocation experiments in SiN nanopores.<sup>47,48</sup> Interestingly, a third high-amplitude peak at a current blockage value of  $\sim 18$  nA is also observed in Figure 6c. This may correspond to the simultaneous transport of multiple RecA-coated DNA molecules through the nanopore.

These results confirm the ability to detect protein-bound DNA complexes using a multilayered graphene- $\text{Al}_2\text{O}_3$  nanopore. Coating dsDNA with a highly stable protein such as RecA significantly improves the SNR of the sensor and affords the flexibility of working with larger 25–30 nm pores, which can be mass-produced using electron beam or nanoimprint lithography. By further reducing membrane thickness ( $d_1$  and  $d_2$  thicknesses in the graphene- $\text{Al}_2\text{O}_3$  stack), biomolecule sensitivity can likely be improved significantly<sup>49</sup> with the eventual goal of detecting and spatially mapping single bound proteins on a DNA molecule.

## CONCLUSION

In summary, this work presents the development of a multilayered graphene- $\text{Al}_2\text{O}_3$  nanopore platform

for the sensitive detection of DNA and DNA–protein complexes at the single-molecule level. The architecture described here is mechanically robust, exhibits low electrical noise, is highly sensitive to electrolyte pH, and allows for the biasing of embedded graphene layers for three-terminal nanopore measurements. Single-molecule transport studies through graphene- $\text{Al}_2\text{O}_3$  nanopores successfully resolved the folded and unfolded translocation of  $\lambda$ -DNA in addition to the transport of RecA-coated DNA, the protein–DNA complex exhibiting significantly deeper ionic current blockades relative to native dsDNA. The robustness and versatility of this architecture gives rise to many interesting future studies. The possibility of regulating ionic current and DNA translocation velocity using a three-terminal nanopore architecture with an embedded, atomically thin graphene gate is particularly intriguing, as high DNA translocation velocities currently limit the utility of solid-state nanopores in DNA sequencing applications. Other exciting possibilities also exist including the fabrication of graphene ribbons and nanogaps in the graphene device layer ( $g_2$ ), enabling the development of novel nanopore structures and sensing modalities for medical diagnostics and sequencing.

## METHODS

**Graphene Growth and Transfer.** Graphene is grown by chemical vapor deposition in an Atomate CVD furnace on 1.4 mil copper foils purchased from Basic Copper (item #: 0014mil-6in $\times$ 4ft).<sup>24,50</sup> An approximately 1  $\times$  3 in. piece of the foil wrapped around a quartz sample holder is annealed under Ar/ $\text{H}_2$  flow for 45 min, and graphene is grown under a  $\text{CH}_4$  (200 sccm) and  $\text{H}_2$  (50 sccm) flow at 1000  $^\circ\text{C}$ ,  $\sim 500$  mTorr for 20 min. The resulting Cu/graphene substrates are cooled to room temperature under Ar flow at a rate of  $\sim 20$   $^\circ\text{C}/\text{min}$ . Transfer to the receiving substrate proceeds as follows: graphene is coated with a bilayer of PMMA (495 K A4 and 950 K A4). Each layer of PMMA is coated at 3000 rpm followed by a 200  $^\circ\text{C}$  bake for 2 min. The backside graphene on the copper foil is removed in an  $\text{O}_2$  plasma (100 W, 20 sccm  $\text{O}_2$ , 30 s) prior to etching the copper in a 0.5 M  $\text{FeCl}_3$  solution overnight. The resultant PMMA/graphene film is wicked onto a Piranha-cleaned glass slide and transferred to a DI water rinse for  $\sim 10$  min. The film is then transferred to a 10% HCl in DI solution to remove residual metal particles, followed by another DI rinse. Finally the film is wicked onto the receiving substrate. After the graphene dries on the receiving substrate ( $\sim 1$  h at room temperature), PMMA is removed in a 1:1 methylene chloride/methanol solution for 20 min. The samples are then placed back in the CVD furnace and annealed at 400  $^\circ\text{C}$  under Ar (500 sccm) and  $\text{H}_2$  (100 sccm) flow to remove residual PMMA. Raman characterization of the film is done using a Renishaw confocal micro-Raman system with a 633 nm HeNe laser at low power to avoid inducing defects and heating in the graphene films. TEM characterization is done using a JEOL 2010F field emission gun TEM.

**Membrane and Nanopore Fabrication.** The  $\text{Al}_2\text{O}_3$  membrane fabrication process has been described in detail previously.<sup>20,21</sup> The free-standing  $\text{Al}_2\text{O}_3$  membrane consists of 700  $\text{\AA}$  of ALD  $\text{Al}_2\text{O}_3$ , deposited at a platen temperature of 250  $^\circ\text{C}$  using tetramethylaluminum (TMA) as the metal precursor and water vapor as the oxygen precursor. The same ALD process is used to deposit

$\text{Al}_2\text{O}_3$  dielectric layers 1 and 2 in the graphene- $\text{Al}_2\text{O}_3$  stack. Nanopores of varying diameter are formed in graphene- $\text{Al}_2\text{O}_3$  membranes using a focused electron beam from a JEOL 2010F field-emission gun TEM operated at 197 kV in convergent beam electron diffraction mode. A focused electron probe with full width at half-maximum (fwhm) of 2.7 nm and beam current density of  $4.2 \times 10^6$  A/m<sup>2</sup> is used to form sub-15 nm diameter nanopores. Nanopores with diameters  $> 15$  nm are formed using a 3.9 nm diameter fwhm probe at a beam current density of  $1.2 \times 10^7$  A/m<sup>2</sup>. Large, 300–350 nm nanopores in  $\text{Al}_2\text{O}_3$  membranes are formed using a FEI DB235 focused ion beam tool operated at a beam current of 30 pA.

**Nanopore Fluidic Measurements.** Prior to fluidic measurements, nanopores are  $\text{O}_2$  plasma treated on the chip backside for 1 min at 50 W. The treated pores are immediately mounted between two chambers of a Delrin flow cell, and 1 M KCl, 10 mM Tris, 1 mM EDTA electrolyte is introduced into both reservoirs. Immediate wetting and ionic conduction through the pore is generally observed. Pores that did not wet immediately were  $\text{O}_2$  plasma treated once more and then wetted with a 50% ethanol, 50% electrolyte solution. All solutions were filtered using a 0.2  $\mu\text{m}$  lure lock filter to remove any large-particulate contamination. Current was measured by placing newly chlorided Ag/AgCl electrodes in each reservoir with the nanopore forming the only electrical/fluidic connection between the two compartments of the flow cell. The entire setup is housed in a double Faraday cage with a dedicated low-noise ground connection, all mounted on a vibration isolation table. The current signal is measured using the Axopatch 200B low-noise current amplifier (Axon Instruments, USA) operated in resistive feedback mode with  $\beta = 1$ . Data are low-pass-filtered at 10 kHz using the built-in 8-pole Bessel filter. The output signal is sent to a Digidata 1440A data-acquisition module (Axon Instruments, USA) and is digitized at 200 kHz and recorded using pClamp 10.2 software. Open pore current is recorded prior to the insertion of dsDNA. DNA translocation studies involved the use of  $\lambda$ -DNA



(New England Biolabs, catalog #: N3011S). RecA-coated DNA was prepared in-house by NABsys Inc. (Providence, RI, USA).

**Electrostatic Simulations.** The mathematical model for ion transport through the pore involves solving equations coupling ionic transport, electric potential, and fluid flow. The details of this process are provided by Jin *et al.*<sup>51</sup> The total flux of the *i*th species (ion) is given by the following expression:

$$\Gamma_i = -D_i \nabla c_i - \Omega_i z_i F c_i \nabla \phi + c_i \mathbf{u} \quad (3)$$

where  $F$  is the Faraday constant,  $z_i$  is the valence,  $D_i$  is the diffusion coefficient,  $\Omega_i$  is the ionic mobility,  $\Gamma_i$  is the flux,  $c_i$  is the concentration of the *i*th species,  $\mathbf{u}$  is the velocity vector of the fluid flow, and  $\phi$  is the electrical potential. The three terms on the right-hand side of eq 3 define the fluxes due to diffusion, electromigration, and convection, respectively. The Nernst–Planck equation describes the transfer of each dissolved species and is given by

$$\frac{\partial c_i}{\partial t} = -\nabla \cdot \Gamma_i \quad (4)$$

The electrical potential distribution is governed by the Poisson equation:

$$\nabla \cdot (\epsilon_r \nabla \phi) = -\frac{F \sum z_i c_i}{\epsilon_0} \quad (5)$$

where  $\epsilon_0$  is the permittivity of vacuum and  $\epsilon_r$  is the relative permittivity. The electric potential at the wall surface is governed by

$$\frac{\partial \phi}{\partial n} = -\frac{\sigma_s}{\epsilon_0 \epsilon_r} \quad (6)$$

where  $\sigma_s$  is the surface charge density and  $n$  is the normal direction of the wall. At pH 8, low surface charge density is assumed ( $|\sigma_s| = 10 \text{ mC/m}^2$ ). The fluid flow is governed by the Navier–Stokes and continuity equations:

$$\rho \left( \frac{\partial \mathbf{u}}{\partial t} + \mathbf{u} \cdot \nabla \mathbf{u} \right) = -\nabla p + \mu \nabla^2 \mathbf{u} - \rho_e \nabla \phi \quad (7)$$

$$\nabla \cdot \mathbf{u} = 0 \quad (8)$$

where  $p$  is the hydrostatic pressure,  $\mu$  is the fluid viscosity, and  $\rho_e$  is the space charge density. From solving the coupled Poisson–Nernst–Planck equations and the Navier–Stokes equations, we can obtain the electric potential, ionic concentration, velocity, and pressure profiles in the nanopore. In the simulations, we assume nonslip boundary conditions and zero normal flux of all the dissolved species on the channel walls. Water dissociation is not considered since the current is dominated by the salt ions. The current through the channel is calculated by integrating the ionic fluxes over the cross-sectional area of the channel (pore area extracted from TEM images), *i.e.*,

$$I = \int_S \sum_i z_i F \Gamma_i \cdot \mathbf{n} dS \quad (9)$$

where  $S$  is the cross-sectional area of the pore.

**Acknowledgment.** The authors would like to acknowledge support from the National Institutes of Health (R21 CA155863) and the Office of Naval Research (ONR). B.M.V. was a trainee supported by the Midwestern Cancer Nanotechnology Training Center (NIH-NCI R25 CA154015) at UIUC. V.E.D. and D.E. acknowledge support from NSF and NDSEG Graduate Research Fellowships, respectively. S.B. was supported by NIH R21 CA155863, and X.J. was supported by NSF Grant 0915718. We also acknowledge NABsys (Providence, RI, USA) for providing the RecA-coated DNA molecules and Dr. Jiwook Shim at UIUC for assistance in noise measurements.

**Supporting Information Available:** Measurements of 1/f noise for Al<sub>2</sub>O<sub>3</sub>, graphene only, and stacked graphene-Al<sub>2</sub>O<sub>3</sub> nanopores, a description of three terminal measurements, and high temporal resolution current traces of DNA and DNA–protein

complex translocation. This material is available free of charge via the Internet at <http://pubs.acs.org>.

## REFERENCES AND NOTES

- Branton, D.; Deamer, D. W.; Marziali, A.; Bayley, H.; Benner, S. A.; Butler, T.; Di Ventra, M.; Garaj, S.; Hibbs, A.; Huang, X.; *et al.* The Potential and Challenges of Nanopore Sequencing. *Nat. Biotechnol.* **2008**, *26*, 1146–1153.
- Venkatesan, B. M.; Bashir, R. Nanopore Sensors for Nucleic Acid Analysis. *Nat. Nanotechnol.* **2011**, *6*, 615–624.
- Geim, A. K. Graphene: Status and Prospects. *Science* **2009**, *324*, 1530–1534.
- Garaj, S.; Hubbard, W.; Reina, A.; Kong, J.; Branton, D.; Golovchenko, J. A. Graphene as a Subnanometre Trans-Electrode Membrane. *Nature* **2010**, *467*, 190–193.
- Merchant, C. A.; Healy, K.; Wanunu, M.; Ray, V.; Peterman, N.; Bartel, J.; Fischbein, M. D.; Venta, K.; Luo, Z. T.; Johnson, A. T. C.; *et al.* DNA Translocation through Graphene Nanopores. *Nano Lett.* **2010**, *10*, 2915–2921.
- Schneider, G. F.; Kowalczyk, S. W.; Calado, V. E.; Pandraud, G.; Zandbergen, H. W.; Vandersypen, L. M. K.; Dekker, C. DNA Translocation through Graphene Nanopores. *Nano Lett.* **2010**, *10*, 3163–3167.
- Min, S. K.; Kim, W. Y.; Cho, Y.; Kim, K. S. Fast DNA Sequencing with a Graphene-Based Nanochannel Device. *Nat. Nanotechnol.* **2011**, *6*, 162–165.
- Nelson, T.; Zhang, B.; Prezhdo, O. V. Detection of Nucleic Acids with Graphene Nanopores: Ab Initio Characterization of a Novel Sequencing Device. *Nano Lett.* **2010**, *10*, 3237–3242.
- Postma, H. W. C. Rapid Sequencing of Individual DNA Molecules in Graphene Nanogaps. *Nano Lett.* **2010**, *10*, 420–425.
- Prasongkit, J.; Grigoriev, A.; Pathak, B.; Ahuja, R.; Scheicher, R. H. Transverse Conductance of DNA Nucleotides in a Graphene Nanogap from First Principles. *Nano Lett.* **2011**, *11*, 1941–1945.
- Valota, A. T.; Kinloch, I. A.; Novoselov, K. S.; Casiraghi, C.; Eckmann, A.; Hill, E. W.; Dryfe, R. A. W. Electrochemical Behavior of Monolayer and Bilayer Graphene. *ACS Nano* **2011**.
- Luan, B.; Peng, H.; Polonsky, S.; Rossmagel, S.; Stolovitzky, G.; Martyna, G. Base-by-Base Ratcheting of Single Stranded DNA Through a Solid-State Nanopore. *Phys. Rev. Lett.* **2010**, *104*, 238103.
- Geim, A. K.; Novoselov, K. S. The Rise of Graphene. *Nat. Mater.* **2007**, *6*, 183–191.
- Liao, A. D.; Wu, J. Z.; Wang, X.; Tahy, K.; Jena, D.; Dai, H.; Pop, E. Thermally Limited Current Carrying Ability of Graphene Nanoribbons. *Phys. Rev. Lett.* **2011**, *106*, 256801.
- Zhi-me, Q.; Shanhong, X.; Haoshen, Z. Slow Spontaneous Transformation of the Morphology of Ultrathin Gold Films Characterized by Localized Surface Plasmon Resonance Spectroscopy. *Nanotechnology* **2009**, *20*, 255702.
- Durkan, C.; Welland, M. E. Analysis of Failure Mechanisms in Electrically Stressed Gold Nanowires. *Ultramicroscopy* **2000**, *82*, 125–133.
- Girit, Ç. Ö.; Meyer, J. C.; Erni, R.; Rossell, M. D.; Kisielowski, C.; Yang, L.; Park, C.-H.; Crommie, M. F.; Cohen, M. L.; Louie, S. G.; *et al.* Graphene at the Edge: Stability and Dynamics. *Science* **2009**, *323*, 1705–1708.
- Zhijun, J.; Mirna, M.; Jason, C.; Derek, S. Fabrication of Nanopores with Embedded Annular Electrodes and Transverse Carbon Nanotube Electrodes. *J. Phys.: Condens. Matter* **2010**, *22*, 454114.
- Bauer, W.; Sosin, A. Point Defect Studies in Gold by Electron Irradiation at Low Temperatures. I. Threshold Displacement Energy and Displacement Cross Section. *Phys. Rev.* **1964**, *135*, A521–A526.
- Venkatesan, B. M.; Dorvel, B.; Yemencioğlu, S.; Watkins, N.; Petrov, I.; Bashir, R. Highly Sensitive, Mechanically Stable Nanopore Sensors for DNA Analysis. *Adv. Mater.* **2009**, *21*, 2771–2776.

21. Venkatesan, B. M.; Polans, J.; Comer, J.; Sridhar, S.; Wendell, D.; Aksimentiev, A.; Bashir, R. Lipid Bilayer Coated Al<sub>2</sub>O<sub>3</sub> Nanopore Sensors: Towards a Hybrid Biological Solid-State Nanopore. *Biomed. Microdevices* **2011**, *13*, 671–682.
22. Dan, Y.; Lu, Y.; Kybert, N. J.; Luo, Z.; Johnson, A. T. C. Intrinsic Response of Graphene Vapor Sensors. *Nano Lett.* **2009**, *9*, 1472–1475.
23. Li, X.; Cai, W.; An, J.; Kim, S.; Nah, J.; Yang, D.; Piner, R.; Velamakanni, A.; Jung, I.; Tutuc, E.; *et al.* Large-Area Synthesis of High-Quality and Uniform Graphene Films on Copper Foils. *Science* **2009**, *324*, 1312–1314.
24. Salehi-Khojin, A.; Estrada, D.; Lin, K. Y.; Bae, M. H.; Xiong, F.; Pop, E.; Masel, R. I. Polycrystalline Graphene Ribbons as Chemiresistors. *Adv. Mater.* **2011**, advanced online publication, DOI: 10.1002/adma.201102663.
25. George, S. M. Atomic Layer Deposition: An Overview. *Chem. Rev.* **2009**, *110*, 111–131.
26. Kim, S.; Nah, J.; Jo, I.; Shahrjerdi, D.; Colombo, L.; Yao, Z.; Tutuc, E.; Banerjee, S. K. Realization of a High Mobility Dual-Gated Graphene Field-Effect Transistor with Al<sub>2</sub>O<sub>3</sub> Dielectric. *Appl. Phys. Lett.* **2009**, *94*, 062107.
27. Liao, L.; Lin, Y.-C.; Bao, M.; Cheng, R.; Bai, J.; Liu, Y.; Qu, Y.; Wang, K. L.; Huang, Y.; Duan, X. High-Speed Graphene Transistors with a Self-Aligned Nanowire Gate. *Nature* **2010**, *467*, 305–308.
28. Fu, W.; Nef, C.; Knopfmacher, O.; Tarasov, A.; Weiss, M.; Calame, M.; Schönenberger, C. Graphene Transistors Are Insensitive to pH Changes in Solution. *Nano Lett.* **2011**, *11*, 3597–3600.
29. Venkatesan, B. M.; Shah, A. B.; Zuo, J. M.; Bashir, R. DNA Sensing Using Nanocrystalline Surface-Enhanced Al<sub>2</sub>O<sub>3</sub> Nanopore Sensors. *Adv. Funct. Mater.* **2010**, *20*, 1266–1275.
30. Harrer, S.; Waggoner, P. S.; Luan, B.; Afzali-Ardakani, A.; Goldfarb, D. L.; Peng, H.; Martyna, G.; Rossnagel, S. M.; Stolovitzky, G. A. Electrochemical Protection of Thin Film Electrodes in Solid-State Nanopores. *Nanotechnology* **2011**, *22*, 275304.
31. Jiang, Z.; Stein, D. Charge Regulation in Nanopore Ionic Field-Effect Transistors. *Phys. Rev. E* **2011**, *83*, 031203.
32. Liu, Y.; Huber, D. E.; Tabard-Cossa, V.; Dutton, R. W. De-screening of Field Effect in Electrically Gated Nanopores. *Appl. Phys. Lett.* **2010**, *97*, 143109–3.
33. Nam, S.-W.; Rooks, M. J.; Kim, K.-B.; Rossnagel, S. M. Ionic Field Effect Transistors with Sub-10 nm Multiple Nanopores. *Nano Lett.* **2009**, *9*, 2044–2048.
34. Kim, R.-H.; Bae, M.-H.; Kim, D. G.; Cheng, H.; Kim, B. H.; Kim, D.-H.; Li, M.; Wu, J.; Du, F.; Kim, H.-S.; *et al.* Stretchable, Transparent Graphene Interconnects for Arrays of Microscale Inorganic Light Emitting Diodes on Rubber Substrates. *Nano Lett.* **2011**, *11*, 3881–3886.
35. Smeets, R. M. M.; Keyser, U. F.; Krapf, D.; Wu, M.-Y.; Dekker, N. H.; Dekker, C. Salt Dependence of Ion Transport and DNA Translocation through Solid-State Nanopores. *Nano Lett.* **2006**, *6*, 89–95.
36. Wanunu, M.; Meller, A. Chemically Modified Solid-State Nanopores. *Nano Lett.* **2007**, *7*, 1580–1585.
37. Stein, D.; Kruithof, M.; Dekker, C. Surface-Charge-Governed Ion Transport in Nanofluidic Channels. *Phys. Rev. Lett.* **2004**, *93*, 035901.
38. Knopfmacher, O.; Tarasov, A.; Fu, W.; Wipf, M.; Niesen, B.; Calame, M.; Schönenberger, C. Nernst Limit in Dual-Gated Si-Nanowire FET Sensors. *Nano Lett.* **2010**, *10*, 2268–2274.
39. Kim, B. G.; Choi, S. K.; Chung, H. S. Dispersing Characteristics of Graphite Suspension by Surface Modification with ABDM. *Part. Sci. Technol.* **2002**, *20*, 95–107.
40. Kimoto, K.; Isakozawa, S.; Aoyama, T.; Matsui, Y. Spatially Resolved EELS Analysis of Multilayer Using EFTEM and STEM. *J. Electron Microsc.* **2001**, *50*, 523–528.
41. Wu, M. Y.; Krapf, D.; Zandbergen, M.; Zandbergen, H. W.; Batson, P. E. Formation of Nanopores in a SiN/SiO<sub>2</sub> Membrane with an Electron Beam. *Appl. Phys. Lett.* **2005**, *87*, 113106–3.
42. Wu, M. Y.; Smeets, R. M. M.; Zandbergen, M.; Ziese, U.; Krapf, D.; Batson, P. E.; Dekker, N. H.; Dekker, C.; Zandbergen, H. W. Control of Shape and Material Composition of Solid-State Nanopores. *Nano Lett.* **2009**, *9*, 479–484.
43. Rothberg, J. M.; Hinz, W.; Rearick, T. M.; Schultz, J.; Mileski, W.; Davey, M.; Leamon, J. H.; Johnson, K.; Milgrew, M. J.; Edwards, M.; *et al.* An Integrated Semiconductor Device Enabling Non-Optical Genome Sequencing. *Nature* **2011**, *475*, 348–352.
44. Li, J.; Gershow, M.; Stein, D.; Brandin, E.; Golovchenko, J. A. DNA Molecules and Configurations in a Solid-State Nanopore Microscope. *Nat. Mater.* **2003**, *2*, 611–615.
45. Storm, A. J.; Storm, C.; Chen, J.; Zandbergen, H.; Joanny, J.-F.; Dekker, C. Fast DNA Translocation through a Solid-State Nanopore. *Nano Lett.* **2005**, *5*, 1193–1197.
46. Wanunu, M.; Sutin, J.; McNally, B.; Chow, A.; Meller, A. DNA Translocation Governed by Interactions with Solid-State Nanopores. *Biophys. J.* **2008**, *95*, 4716–4725.
47. Smeets, R. M. M.; Kowalczyk, S. W.; Hall, A. R.; Dekker, N. H.; Dekker, C. Translocation of RecA-Coated Double-Stranded DNA through Solid-State Nanopores. *Nano Lett.* **2008**, *9*, 3089–3095.
48. Kowalczyk, S. W.; Hall, A. R.; Dekker, C. Detection of Local Protein Structures along DNA Using Solid-State Nanopores. *Nano Lett.* **2009**, *10*, 324–328.
49. Wanunu, M.; Dadosh, T.; Ray, V.; Jin, J. M.; McReynolds, L.; Drndic, M. Rapid Electronic Detection of Probe-Specific MicroRNAs Using Thin Nanopore Sensors. *Nat. Nanotechnol.* **2010**, *5*, 807–814.
50. Wood, J. D.; Schmucker, S. W.; Lyons, A. S.; Pop, E.; Lyding, J. W. Effects of Polycrystalline Cu Substrate on Graphene Growth by Chemical Vapor Deposition. *Nano Lett.* **2011**, *11*, 4547–4554.
51. Jin, X.; Aluru, N. Gated Transport in Nanofluidic Devices. *Microfluid. Nanofluid.* **2011**, *11*, 297–306.